PHYSICAL REVIEW B **86**, 174114 (2012)

Atomic structure relaxation in nanocrystalline NiO studied by EXAFS spectroscopy: Role of nickel vacancies

A. Anspoks,[*] A. Kalinko,[†] R. Kalendarev,[‡] and A. Kuzmin[§]
Institute of Solid State Physics, University of Latvia, Kengaraga street 8, LV-1063 Riga, Latvia

(Received 4 June 2012; published 26 November 2012)

Nanocrystalline NiO samples have been studied using the Ni K-edge extended x-ray absorption fine structure (EXAFS) spectroscopy and recently developed modeling technique, combining classical molecular dynamics with *ab initio* multiple-scattering EXAFS calculations (MD-EXAFS). Conventional analysis of the EXAFS signals from the first two coordination shells of nickel revealed that (i) the second shell average distance R(Ni–Ni$_2$) expands in nanocrystalline NiO compared to microcrystalline NiO, in agreement with overall unit cell volume expansion observed by x-ray diffraction; (ii) on the contrary, the first shell average distance R(Ni–O$_1$) in nanocrystalline NiO shrinks compared to microcrystalline NiO; (iii) the thermal contribution into the mean-square relative displacement σ^2 is close in both microcrystalline and nanocrystalline NiO and can be described by the Debye model; (iv) the static disorder is additionally present in nanocrystalline NiO in both the first Ni–O$_1$ and second Ni–Ni$_2$ shells due to nanocrystal structure relaxation. Within the MD-EXAFS method, the force-field potential models have been developed for nanosized NiO using as a criterion the agreement between the experimental and theoretical EXAFS spectra. The best solutions have been obtained for the 3D cubic-shaped nanoparticle models with nonzero Ni vacancy concentration C_{vac}: $C_{\text{vac}} \approx 0.4$–$1.2\%$ for NiO nanoparticles having the cube size of $L \approx 3.6$–4.2 nm and $C_{\text{vac}} \approx 1.6$–$2.0\%$ for NiO thin film composed of cubic nanograins with a size of $L \approx 1.3$–2.1 nm. Thus our results show that the Ni vacancies in nanosized NiO play important role in its atomic structure relaxation along with the size reduction effect.

DOI: 10.1103/PhysRevB.86.174114 PACS number(s): 61.05.cj, 78.70.Dm, 61.72.jd, 61.46.Hk

I. INTRODUCTION

In the past, significant efforts have been devoted to the preparation of metal oxide functional nanomaterials with tailored properties.[1] Different physical and chemical preparation methods influence on the final product, in particular, its stoichiometry, metal oxidation state, the presence of impurities as well as coexistence of amorphous and crystalline phases.[2] A key requirement for understanding and control of nanomaterial properties is the knowledge of its atomic structure, whose determination is a challenging task. It can be addressed by a complex modeling approach based on an effective combination of the experimental methods and the theory.[3]

While different experimental techniques exist to study nanomaterials,[2,4] only two methods, namely total scattering[5] and x-ray absorption spectroscopy (XAS),[6,7] provide with direct access to the structural information. XAS is an excellent tool for this purpose, because it is element selective, sensitive to low element concentration, and scales down to nanoparticles and even molecules.[8–10] The possibility to perform XAS experiments with the spatial resolution at nanoscale has been also demonstrated recently.[11,12]

Being a local probe, XAS gives an insight into the atomic structure of a material within about 3–10 Å around the absorbing atom.[10] The structural information is encrypted within the oscillating part of x-ray absorption coefficient, the so-called extended x-ray absorption fine structure (EXAFS), located above the absorption edge of an element.[13,14] Contrary to the total scattering method,[5] which is sensitive to the atomic pair distribution functions (PDFs), the EXAFS includes contributions from many-atom distributions, known as the multiple-scattering (MS) effects, being sensitive not only to the interatomic distances, but also to the bonding angles.[15] This fact makes the EXAFS technique unique in a characterization of nanosized and complex functional materials.

The EXAFS theory has been largely improved during the last decades and is rather well developed today.[13,14] However, its application to the analysis of contributions from outer coordination shells into the total EXAFS spectrum is limited by the ability to reliably incorporate thermal disorder and the multiple-scattering effects. This problem is crucial in the case of nanomaterials, where the size reduction effect, leading to the high surface to volume ratio, and its accompanied atomic structure relaxation at the surface and in the bulk of nanoparticles influence strongly the shape of the EXAFS spectrum.[6,7] To deal with this problem, we have developed the MD-EXAFS modeling method combining *ab initio* EXAFS calculations with classical molecular dynamics (MD) simulations.[16] It allows us to generate from the MD run a set of atomic configurations, which are further employed to compute the configuration-averaged EXAFS spectrum using the full power of modern *ab initio* multiple-scattering theory.[14] The method has been successfully applied to the interpretation of EXAFS spectra in several crystalline materials as SrTiO$_3$,[17] ReO$_3$,[18] Ge,[19] and LaCoO$_3$.[20] The important advantage of this method is a small number of model parameters, which are used in the force-field potential to describe interactions between atoms in the material. Note that modern MD simulations can deal with very large number of atoms (even millions),[21,22] allowing one to create realistic models of a nanoobject without any significant limitations.

In this work, we will demonstrate the potentiality of the MD-EXAFS method for the interpretation of the Ni K-edge EXAFS in nanocrystalline nickel oxide (NiO). NiO represents challenging example of nanomaterial, which finds a broad range of practical applications including but not limited to catalysis, electrochromic devices, gas sensors, resistive and magnetoresistive memory, giant magnetoresistive (GMR) spin valve structures, rechargeable batteries, and fuel cells.[23–29] Note that a performance of all these devices depends largely on the oxide stoichiometry. NiO is known to be p-type semiconductor, having usually an oxygen excess due to the presence of nickel vacancies (V_{Ni}).[30–32]

EXAFS spectroscopy has been used to study nickel oxide for a long time.[33–36] Most works have been dedicated to an investigation of NiO thin films. The in-plane and out-of-plane strains have been evaluated in the epitaxial ultrathin NiO layers on Ag(001) in Refs. 37–39. A decrease of the first shell average distance R(Ni–O$_1$) by ∼0.02–0.04 Å and an increases of the mean second shell distance R(Ni–Ni$_2$) by ∼0.01–0.02 Å have been observed in pure $\mathrm{Ni}_{1-x}\mathrm{O}$ and vanadium doped $\mathrm{Ni}_{1-x}\mathrm{V}_x\mathrm{O}_y$ thin films.[40,41] Recently, the presence and the role of nickel vacancies have been studied in sputtered NiO films.[42,43] It was concluded that nickel vacancies, being the dominant point defects, are responsible for the electrical conductivity of the films[42] and for the film decomposition under annealing in vacuum above 400 °C.[43] At the same time, very few works exist to our knowledge on the EXAFS studies of NiO nanoparticles. An elongation of the first shell R(Ni–O$_1$) and second shell R(Ni–Ni$_2$) distances has been found in ultra fine NiO particles dispersed on activated carbon fibers.[44] *In-situ* EXAFS study of the initial crystallization stage of NiO nanoparticles from the amorphous precursor has been performed in Ref. 45. Finally, the influence of point defects in NiO nanoparticles has been studied recently in relation to their magnetic properties.[46] It has been proposed that a distribution of nickel vacancies in NiO nanoparticles, having the size between 10 and 18 nm, can be considered within the core-shell model.[46]

Note that most previous EXAFS studies have been limited to the analysis of the first two coordination shells of nickel, thus excluding large amount of experimental data from the analysis. A more rigorous approach, based on the MD-EXAFS method,[16] has been used by us recently to study the structure relaxation and lattice dynamics in nanocrystalline (13 nm) NiO powder in comparison with microcrystalline oxide.[47,48] In our previous works,[47,48] only the size reduction effect and related atomic structure relaxation have been considered when simulating nanocrystalline NiO. The developed force-field (FF) potential model allowed us to reproduce well within the multiple-scattering approach the Ni K-edge EXAFS spectrum of microcrystalline NiO, taking into account the contributions from the first six coordination shells (up to ∼5.5 Å).[47,48] However, the same force-field model, applied to nanocrystalline NiO, predicted opposite direction of the relaxation for the first coordination shell of nickel compared to the results of conventional EXAFS data analysis based on the best fitting procedure.[47,48] Thus we concluded that the model, developed for microcrystalline NiO, should be improved to describe correctly the atomic structure of nanocrystalline NiO.

Therefore a more advanced model, additionally taking into account the presence of nickel vacancies, has been developed in the present work, based on the results of temperature dependent (from 10 to 300 K) Ni K-edge EXAFS experiments for microcrystalline, nanocrystalline powder and thin film NiO samples. As we will show below, the new model predicts correctly a relaxation of the first and outer coordination shells in nanocrystalline NiO upon its size reduction giving simultaneously good agreement between the configuration-averaged and experimental Ni K-edge EXAFS spectra within the multiple-scattering approximation. Moreover, the model allows to estimate an amount of nickel vacancies, being directly responsible for the first shell relaxation in the bulk of nanocrystals.

The paper is organized as follows. In Sec. II, we describe the preparation of samples, EXAFS experiments and conventional data analysis procedure. The details of the MD-EXAFS simulation method are explained in Sec. III. The obtained results, using both conventional and MD-EXAFS approaches, are presented and discussed in Sec. IV.

II. EXPERIMENTAL AND DATA ANALYSIS

In the present work we studied two different nickel oxide nanocrystalline samples (powder and thin film) in comparison with commercial microcrystalline NiO powder (c-NiO, Aldrich, 99%), having green color. Black color of nanopowder and dark brown color of the thin film indicate the presence of nickel vacancies.[30,49,50]

Nanocrystalline $\mathrm{Ni}_{1-x}\mathrm{O}$ powder (nano-NiO) was produced by the precipitation method,[51] based on a reaction of aqueous solutions of $\mathrm{Ni(NO_3)_2{\cdot}6H_2O}$ and NaOH, followed by subsequent annealing of the precipitate in air at 250 °C. Nanocrystalline $\mathrm{Ni}_{1-x}\mathrm{O}$ thin film (tf-NiO) was produced using reactive dc-magnetron sputtering of metallic nickel target in mixed Ar-O$_2$ atmosphere (gas ratio Ar:O$_2$ = 9:1) on polyimide tape. According to the x-ray diffraction data, the Scherrer's method and assuming the cubic crystallites shape, the average size of nanocrystallites was 6.2 ± 1.8 nm in the nanopowder and 5.9 ± 0.9 nm in the thin film.

The Ni K-edge x-ray absorption spectra were measured in transmission mode at the HASYLAB/DESY C1 bending-magnet beamline in the temperature range from 6 K to 300 K. The storage ring DORIS III operated at $E = 4.44$ GeV and $I_{\max} = 140$ mA. The x-ray radiation was monochromatized by a 40% detuned Si(111) double-crystal monochromator, and the beam intensity was measured using two ionization chambers filled with argon and krypton gases. To achieve the absorption Ni K-edge jump value $\Delta\mu \approx 1$, the proper amount of the NiO powder was deposited on Millipore nitrocellulose membrane filter and fixed by Scotch tape, whereas a stack of simultaneously sputtered thin films was used.

The EXAFS oscillations $\chi(k)$ were extracted and analyzed following the conventional procedure[10] using the EDA software package.[52] The low-temperature experimental EXAFS data $\chi(k)k^2$ and their Fourier transforms are shown in Fig. 1. Note the high quality of the obtained EXAFS data in a wide k-space range up to 18 Å^{-1} for all samples. Noticeable difference between the EXAFS spectra of microcrystalline and nanocrystalline samples is clearly visible due to a reduction of crystallite size (see Fig. 1). The EXAFS spectra for all samples show significant temperature dependence (see the case of nano-NiO in Fig. 2), suggesting that lattice dynamic effects are important and are not masked by structural disorder.

A contribution to the total EXAFS spectrum from the first two coordination shells (the peaks at ∼1.7 and ∼2.7 Å in Fig. 1)

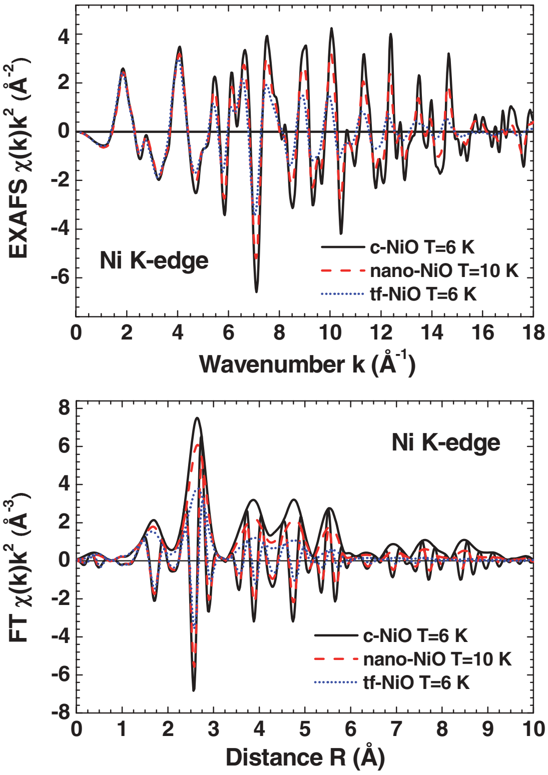

FIG. 1. (Color online) Low-temperature Ni K-edge EXAFS spectra $\chi(k)k^2$ and their Fourier transforms (FTs) for c-NiO, nano-NiO, and tf-NiO.

can be analyzed in the single-scattering approximation.[47,48] Therefore it was isolated by the Fourier filtering procedure in the R-space range of 0.7–3.2 Å and best fitted in the k-space range of 2–17 Å^{-1} using the two-component Gaussian model.[10] The scattering amplitude and phase shift functions for the Ni–O$_1$ and Ni–Ni$_2$ atom pairs, used in the fits, were extracted from the low temperature ($T = 6$ K) experimental data of c-NiO sample, assuming the crystallographic value of the lattice parameter $a_0 = 4.176$ Å.[53] As a result, the temperature dependencies of the mean-square relative displacements (MSRDs) σ^2 and interatomic distances R were obtained and are shown in Figs. 3 and 4, respectively. Note that thus determined MSRD values are relative to the low temperature c-NiO data, i.e., $\Delta\sigma^2 = \sigma^2(T) - \sigma^2(\text{c-NiO}, T = 6\ \text{K})$.

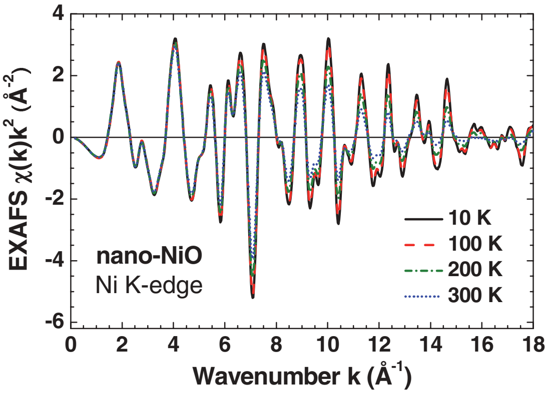

FIG. 2. (Color online) The Ni K-edge EXAFS spectra $\chi(k)k^2$ for nano-NiO at selected temperatures. Thermal disorder leads to the oscillations damping at high-k values.

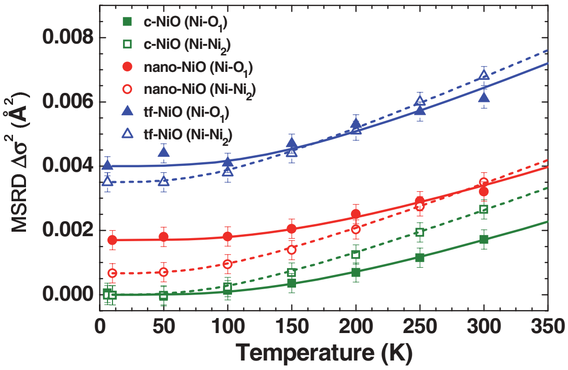

FIG. 3. (Color online) Temperature dependence of the mean-square relative displacements (MSRD) σ^2 for the first (Ni–O$_1$) and second (Ni–Ni$_2$) coordination shells in c-NiO, nano-NiO, and tf-NiO relative to the MSRD value in c-NiO at $T = 6$ K. The Debye models are shown by lines. See text for the values of the characteristic Debye temperatures.

III. MD-EXAFS SIMULATIONS

Analysis of the full EXAFS spectra, including contributions from outer coordination shells, requires a more advanced and elaborated approach, because multiple-scattering effects become important there.[48] A comparison of Fourier transforms of the simulated EXAFS spectra taking into account only single-scattering or all multiple-scattering (up to 8th order) contributions is shown in Fig. 5: they differ at the distances longer than ∼3.2 Å, i.e., above the second peak, thus confirming the importance of the multiple-scattering effects. At the same time, this result confirms that the single-scattering approximation is valid for the first two coordination shells of nickel.

To go beyond the limitations of the conventional EXAFS analysis, we employed a recently developed simulation method,[16,17] combining *ab initio* EXAFS calculations with classical molecular dynamics (MD), further referenced as MD-EXAFS. This approach allows us to reconstruct structural and dynamic information for the coordination shells beyond the second coordination shell taking into account structure

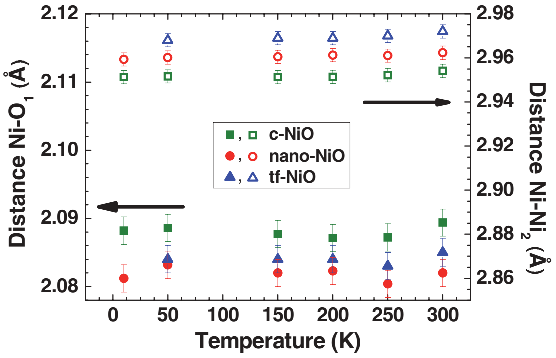

FIG. 4. (Color online) Temperature dependence of the average interatomic distances in the first (Ni–O$_1$) and second (Ni–Ni$_2$) coordination shells of nickel in c-NiO, nano-NiO, and tf-NiO.

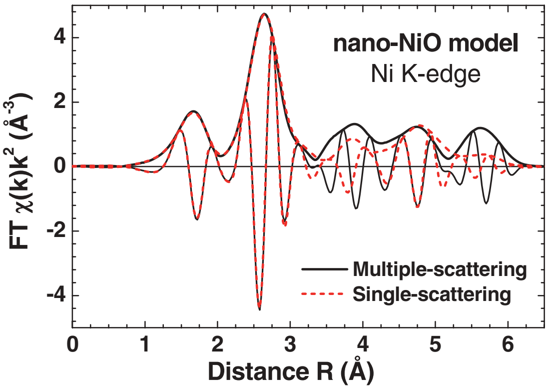

FIG. 5. (Color online) Fourier transforms of the configuration-averaged Ni K-edge EXAFS spectra $\chi(k)k^2$ calculated within the single-scattering and multiple-scattering approximations for a model NiO nanoparticle having a size of $L \approx 4.2$ nm.

relaxation in nanoparticles and the presence of defects (nickel vacancies). Below, we will explain an implementation of the MD-EXAFS scheme for nanoparticles (see Fig. 6) in more details.

A. Nanoparticle model

Before starting MD-EXAFS calculations, one needs to define a structural model of the material. For NiO nanoparticle, this means to specify its shape and size, nickel vacancy concentration, and the force-field (FF) parameters used in the MD simulation.

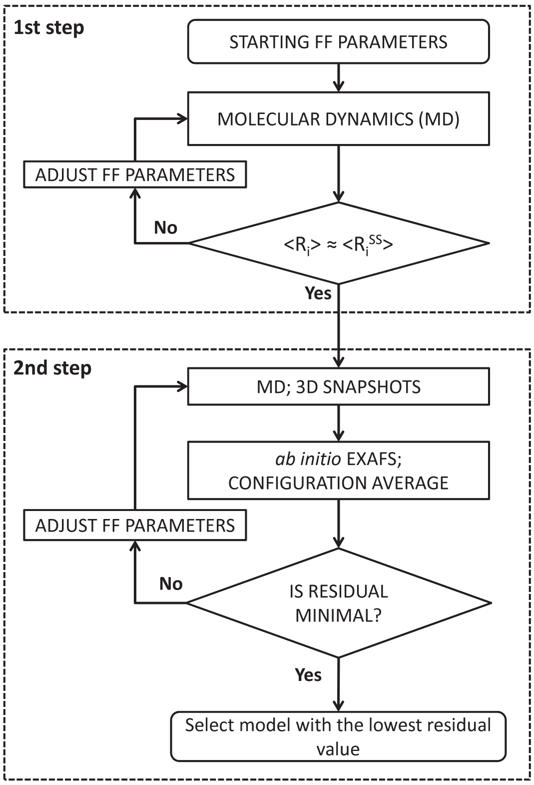

FIG. 6. A scheme of the MD-EXAFS calculation.

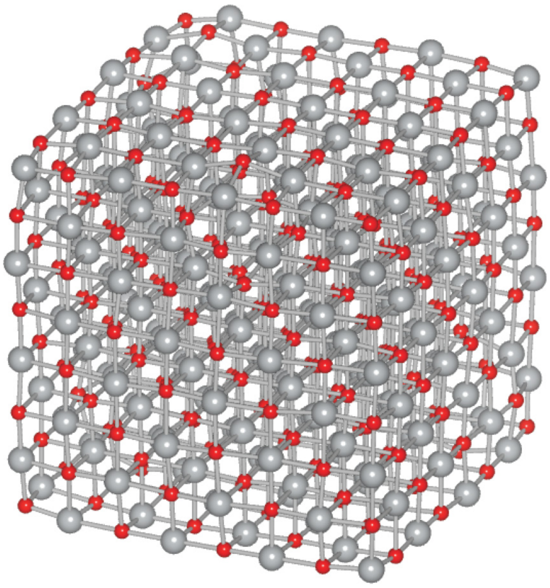

FIG. 7. (Color online) Example of the single MD snaphot of NiO nanoparticle with the size $L = 9$ and four nickel vacancies. Small red balls indicate oxygen atoms; large gray balls correspond to nickel atoms.

Nanosized nickel oxide particles were simulated in the canonical ensemble (NVT) using cubic shape clusters $L \times L \times L$ placed in a large empty box. They were generated from cubic rocksalt-type unit cell having the symmetry $Fm\bar{3}m$ (space group 225) and containing four nickel and four oxygen atoms (see Fig. 7). The cluster size was up to $L = 40a_0$, where $a_0 = 4.1773$ Å is lattice parameter of c-NiO.[56] Thus this model corresponds to the free NiO particle in the vacuum.

The size of the particle and positions of atoms inside it were relaxed during the MD simulation to reach the equilibrium parameters determined by the force-field potential. Nickel vacancies were generated by randomly removing Ni atoms from the model particle, ensuring their homogeneous distribution. Thus each model particle is characterized by its size L and the number of nickel vacancies N_{vac}. Taking into account that

$$N_{\text{Ni}} + N_{\text{vac}} = N_{\text{O}}, \tag{1}$$

the vacancy concentration C_{vac} can be calculated as

$$C_{\text{vac}} = \frac{N_{\text{vac}}}{N_{\text{O}}}, \tag{2}$$

where N_{Ni} and N_{O} are the number of nickel and oxygen atoms, respectively.

Crystalline NiO was modeled in the isothermal-isobaric ensemble (NPT) with constant pressure and temperature using the supercell size $6 \times 6 \times 6$ and 3D periodic boundary conditions. During MD run, this structure was relaxed to its equilibrium position.

Our force-field (FF) potential model included two-body central force interactions between atoms i and j described by a sum of the Buckingham and Coulomb potentials:

$$U_{ij} = A_{ij}\exp(-r_{ij}/\rho_{ij}) - \frac{C_{ij}}{r_{ij}^6} + \frac{Z_i Z_j e^2}{r_{ij}}. \tag{3}$$

TABLE I. Force-field potential parameters of the Buckingham potentials for the Ni–O and O–O atom pairs used in the molecular dynamics simulations.

Pair of atoms	A (eV)	ρ (Å)	C (eVÅ^6)
Ni–O	754.92	0.3277	0.0
O–O	22764.3	0.1490	27.89

The Buckingham potential parameters A, ρ, and C are reported in Table I, they were taken from previous simulations of c-NiO[48,57] and reproduce well properties of bulk crystal using the formal charges of ions ($Z_{Ni} = +2.0$ for nickel atoms and $Z_O = -2.0$ for oxygen atoms).

In this study, we selected the charge of nickel atoms Z_{Ni} as the optimization parameter to minimize the residual between experimental and calculated EXAFS signals. All other Buckingham potential parameters were left unchanged. Such choice is justified by the fact that the lattice dynamics of c-NiO and both nanocrystalline samples is close at all studied temperatures (see Fig. 3), and the difference in the static part of the MSRDs is attributed to atomic structure relaxation. The charge of oxygen atoms Z_O was calculated to maintain electroneutrality of the system, taking into account the Ni vacancies when present:

$$Z_O = -Z_{Ni}\frac{N_{Ni}}{N_O}. \tag{4}$$

Note that in our simple model, all Ni ions have the same charge (Z_{Ni}) and so do all oxygen ions (Z_O).

B. Details of the MD-EXAFS modeling

The advantage of the MD-EXAFS method is a significant reduction of a number of free model parameters, which are required to describe the structure and dynamics of NiO nanoparticles. There are only three such parameters: the size of the particle L, the number of nickel vacancies N_{vac} and the charge of nickel atoms Z_{Ni}. All interatomic distances, bond angles, thermal and static disorder effects are obtained from MD simulations by calculating configuration averages from snapshots of instant atomic positions.

At the first step (see Fig. 6), one needs to perform the MD simulations with the goal to find the values of the force-field parameters that result in the mean values of interatomic distances for the first two coordination shells being in agreement (in our case, within ±0.005 Å) with those obtained from the conventional analysis of the experimental EXAFS spectrum in the single-scattering approximation (see Fig. 4). Note that for our force-field potential model, only one parameter Z_{Ni} should be optimized, and the mean values of $R(\text{Ni–O}_1)$ and $R(\text{Ni–Ni}_2)$ distances were determined from the Ni–O and Ni–Ni pair distribution functions obtained from the MD run.

To understand a behavior of our model and to increase efficiency of the optimization procedure, we studied how the calculated mean distances in the first $R(\text{Ni–O}_1)$ and second $R(\text{Ni–Ni}_2)$ coordination shells depend on the charge of Ni ions. By performing MD simulations, we found that both interatomic distances show linear dependence on the Ni ion charge Z_{Ni}. This result allowed us to save a lot of computing effort, by calculating the value of Z_{Ni}, which provides the desired value of the mean interatomic distance for the first or second coordination shell, from the linear dependence $R(Z_{Ni})$.

Summing up, the first step of the calculations (see Fig. 6) was relatively fast screening procedure to tune the force-field parameter Z_{Ni} for different values of L and N_{vac} and to select only those model particles, which have the mean distances in the first $R(\text{Ni–O}_1)$ and second $R(\text{Ni–Ni}_2)$ coordination shells within the desired agreement (±0.005 Å or better in the present work) with those obtained from the conventional analysis (see Fig. 4).

At the second step (see Fig. 6), the agreement between the configuration-averaged EXAFS spectrum and the experimental EXAFS spectrum, which was Fourier filtered in the range from 0 to 6.5 Å, was used as a goodness of model criterion. The configuration-averaged EXAFS spectrum for the model particle was calculated for a set of snapshots of instant atomic positions generated by MD simulation. Note that for each MD snapshot the averaging of EXAFS spectra over all nickel atoms in the particle was performed. In EXAFS calculations we used full potential of the multiple-scattering theory up to the 8th order and considered contributions from coordination shells up to 6.5 Å around the absorbing nickel atom. Such approach allowed us to take into account disorder effects caused by atomic thermal vibrations and by structure relaxation due to the finite size of the particle and the presence of nickel vacancies. Note that while the charge Z_{Ni} of Ni ions was optimized for each set of L and N_{vac} parameters at the first modeling step, it was additionally tuned around previously determined value by allowing its small (±0.05) variation.

A convergence of the configuration-averaged EXAFS spectrum was controlled by evaluating its variation upon an addition of the successive MD snapshot. The convergence was achieved when a change of the mean square difference between two configuration-averaged EXAFS spectra was below 10^{-4}. This criterion is usually satisfied when one averages over the EXAFS signals from 4000 Ni atoms. For large enough particles, this means that even a single MD snapshot of the particle is enough to create configuration-average EXAFS spectrum. However, for smaller particles one needs many MD snapshots in order to collect 4000 signals and to achieve convergence.

At the end of the second step, for each selected model particle one obtains optimal values of the force-field parameters (only one, Z_{Ni}, in the present case), which lead to the minimal residual between the configuration-averaged and experimental EXAFS spectra. By comparing residual values for the model particles with different size and nickel vacancy concentration, one can select the model particle, which provides the lowest possible residual for the given experimental EXAFS spectrum.

Our modeling procedure allows one to obtain not only the basic structural information like average interatomic distances, bond angles, MSRD values, coordination numbers, pair and many-atom distribution functions, which can be calculated from the atomic coordinates, but also to determine other properties of the model particle like phonon frequencies, elastic properties, etc., using the optimized force-field potential model.[54]

C. Details of the MD and EXAFS calculations

For classical MD simulations we used DLPOLY4.02 code,[55] which is suitable for both crystalline and nanosized materials. The integration of Newton's equations was performed by the leapfrog Verlet method. In each simulation, the structure was first equilibrated during 75 ps at 300 K and zero pressure, corresponding to conditions of the EXAFS experiments, and a set of instantaneous atomic configurations was accumulated during next 20-ps production run with a time step of 0.5–2.0 fs, which is equivalent to the largest allowed change of the distance 0.1 Å during the single time step. The calculated sets of instantaneous atomic configurations were also used to evaluate the total and pair distribution functions. These PDFs were further decomposed into a set of Gaussian functions to evaluate the values of coordination numbers CN, interatomic distances R, and corresponding MSRDs σ^2.

The Ni K-edge EXAFS spectra were calculated for each instantaneous atomic configuration and for all absorber (nickel) atoms in each of these configurations using the *ab initio* real-space multiple-scattering FEFF8 code.[58] The scattering potentials and partial phase shifts were evaluated only once for the average configuration, thus neglecting a variation of the scattering potentials due to a disorder.[16] Since we are interested to account for the contributions from the outer coordination shells, it is important to take into account the multiple-scattering effects.[48] In our calculations, we considered the multiple-scattering contributions up to the eighth order with the half path length up to 6.5 Å. To reduce the number of scattering paths, they were filtered using the cutoff criteria (CRITERIA 0.0 1.7) as is implemented in the FEFF8 code.[58] This means that all paths with the mean amplitude of 1.7% and above of largest path, estimated within the plane wave approximation, were kept. The inelastic losses were taken into account using the complex exchange-correlation Hedin-Lundqvist potential.[14] The cluster potential was of the muffin-tin (MT) type, and the values of the MT radii were $R_{\mathrm{MT}}(Ni) = 1.319$ Å and $R_{\mathrm{MT}}(O) = 1.021$ Å.

IV. RESULTS AND DISCUSSION

Temperature dependencies of the relative MSRDs $\Delta\sigma^2$ and the interatomic distances R, obtained using conventional analysis[10] for the first two coordination shells (O_1 and Ni_2) of nickel, are shown in Figs. 3 and 4, respectively. The difference between temperature dependencies of the MSRDs (see Fig. 3) for nano- and microcrystalline NiO samples remains nearly constant in the whole range of temperatures in both the first and second coordination shells. Its origin is due to the static disorder in nanocrystalline NiO, which is induced by a relaxation of its atomic structure. At the same time, the thermal disorder contribution $\sigma^2(T)$ into the MSRD is close in all samples but differs for the first and second coordination shells, as expected. It can be well described by the Debye model[61] with the following characteristic temperatures: $\theta_D(\mathrm{Ni–O_1}) = 680$ K and $\theta_D(\mathrm{Ni–Ni_2}) = 425$ K for c-NiO; $\theta_D(\mathrm{Ni–O_1}) = 680$ K and $\theta_D(\mathrm{Ni–Ni_2}) = 415$ K for nano-NiO; and $\theta_D(\mathrm{Ni–O_1}) = 600$ K and $\theta_D(\mathrm{Ni–Ni_2}) = 390$ K for tf-NiO. These values are consistent with those, $\theta_D(\mathrm{O}) = 719$ K and $\theta_D(\mathrm{Ni}) = 366$ K, derived in Ref. 62 from the bulk thermal vibration amplitudes of nickel and oxygen atoms, obtained within the simple Debye model by high-resolution 120 keV He^+ ion scattering at room temperature, and also with the results of heat capacity measurements, $\theta_D(\mathrm{O}) = 900$ K and $\theta_D(\mathrm{Ni}) = 425$ K (see Ref. 63), $\theta_D(\mathrm{O}) = 762.5$ K and $\theta_D(\mathrm{Ni}) = 515.9$ K (see Ref. 64).

The average second shell distance $R(\mathrm{Ni–Ni_2})$ in nanocrystalline samples is longer by ~0.01 Å in nano-NiO and by ~0.02 Å in tf-NiO than that in microcrystalline c-NiO at all temperatures (see Fig. 4). This fact is in agreement with the overall unit cell volume expansion upon a decrease of NiO nanocrystals size observed by diffraction.[59,60] On the contrary to the second shell behavior, the average first shell $R(\mathrm{Ni–O_1})$ distance in all nanocrystalline samples is shorter compared with microcrystalline NiO (see Fig. 4). This interesting result has been found by us previously[47,48] in nanosized NiO powder at room temperature and now is confirmed in a wide temperature range for differently prepared NiO nanocrystalline samples. We explored this controversy in the behavior of the first and second shell interatomic distances in details using the MD simulations of nanoparticles.

In our previous works,[47,48] we have considered the model of defect-free cubic NiO nanoparticles. Using such model we have achieved good overall agreement with the experimental Ni K-edge EXAFS data and reproduced the expansion of the unit cell but not the contraction of the first coordination shell radius.

In the defect-free nanoparticles, the only source of the nearest bond $\mathrm{Ni–O_1}$ shortening is a relaxation at nanoparticle surface. The influence of such relaxation on the average $\mathrm{Ni–O_1}$ distance increases upon a decrease of nanoparticle size, because of an increase in the ratio between the number of atoms located at the surface relative to their total number. However, the experimental values of both average distances [$R(\mathrm{Ni–O_1})$ and $R(\mathrm{Ni–Ni_2})$] can be reproduced only for unrealistically small defect-free model of nanoparticle with the size $L = 3a_0 \approx 1.2$ nm. Moreover, this model, being too simple, does not provide a good fit to the experimental EXAFS spectra. Thus one should search for a more elaborated model to explain the experimental results.

The black color of our nanocrystalline samples gives strong evidence of the presence of nickel vacancies,[30,49,50] therefore an apparent step towards an improvement of the nanoparticle model is to introduce the Ni vacancies and to test their influence on the EXAFS spectra and structural parameters.

As we have noted previously,[47] the force-field potential parameters cannot be directly transformed from crystal to nanoparticles, since they lead to incorrect values of interatomic distances and to incorrect relaxation. Thus, their additional optimization is required for nanoparticles. Previously,[47,48] we have varied the ρ(Ni–O) and ρ(O–O) parameters of the Buckingham potential, which determine a position of the potential minimum. The same results can be achieved by changing the charge of ions. One should remember that in the force-field potential model the ion charge is just another parameter to simulate the real interaction between atoms. As we have noted previously, in this study we have selected the charge of nickel atoms Z_{Ni} as the optimization parameter to minimize the residual between the experimental and calculated EXAFS signals.

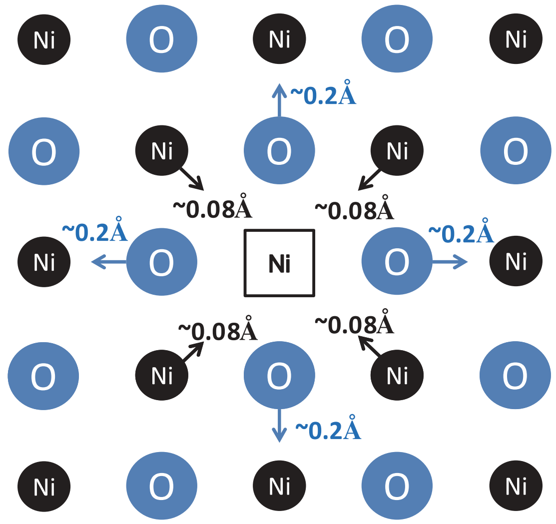

FIG. 8. (Color online) Schematic view of the nearest-neighbor relaxation around nickel vacancy in the bulk of nickel oxide according to our molecular dynamics simulations. Note that oxygen atoms move outwards, but nickel atoms move inwards to the nickel vacancy.

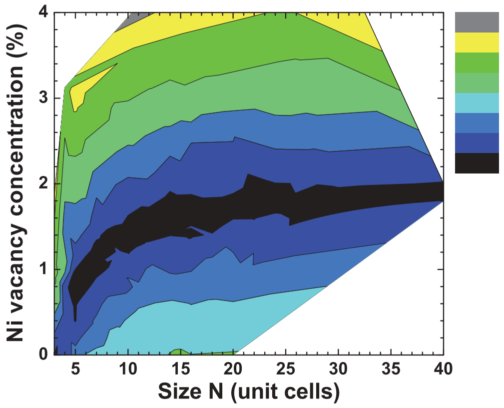

FIG. 9. (Color online) The dependence of the residual modulus value $|\Delta R(\text{Ni–O}_1)|$ between the first shell interatomic distances, obtained for cubic NiO nanoparticles by conventional analysis method (see Fig. 4) and from the MD simulation, on the nickel vacancy concentration C_{vac} and the nanoparticle size $L = Na_0$ under imposed requirement that the second shell interatomic distance $R(\text{Ni–Ni}_2)$ should coincide with the value, obtained by the conventional modeling procedure (see Fig. 4), within ±0.001 Å.

As the first application of previously described MD-EXAFS procedure we optimized the ion charge of nickel in c-NiO. The minimal value of the residual between the calculated and experimental EXAFS spectra was achieved for $Z_{\text{Ni}} = +2.015$ and $Z_{\text{O}} = -2.015$. These values differ only slightly from the initial values ±2.0, that gives us additional confidence in selected procedure and our FF model.

To understand the influence of nickel vacancies on the structure of nanoparticles, we calculated the relaxation of the local atomic structure around the vacancy in the bulk of c-NiO (see Fig. 8). This was done by calculating the average atomic distances for a large set of atomic configurations, generated by the MD simulation. The obtained results show that the six nearest oxygen atoms move away from the center of the vacancy by $\approx$0.2 Å, thus significantly decreasing the distance with the neighboring Ni atoms. At the same time, twelve nearest Ni atoms move slightly towards the center of the vacancy by $\approx$0.08 Å, thus increasing the distance between the nearest Ni atoms.

This relaxation is caused by short-range two-body central force interactions given by Buckingham potential and by long-range Coulomb interactions. By removing a Ni atom one changes the balance of the electrostatic interactions, so it is expected that oppositely charged nickel and oxygen ions move closer, whereas ions having the same charge move apart from each other. This effect is strong in the first shell (Ni–O) and becomes much weaker in the second shell, and practically vanishes in the next shells. Such relaxation of atomic structure, induced by the presence of nickel vacancy, plays significant role in the average structure relaxation, especially for the first coordination shell of nickel, as was found recently.[42] The results of our simulations are in excellent agreement with those from the recent *ab initio* calculations[65,66] of the structure relaxation around Ni vacancy, which predict the relaxation of O atoms by about 0.17 Å outwards from the vacancy. This fact confirms the ability of our simple force-field potential model to reproduce well structure relaxation around nickel vacancies.

The structure relaxation within the whole nanoparticle shows a very complex picture. The influence of surface extends deep inside the nanoparticle volume, and, only in the large enough nanoparticles having a size $L >$10 nm, one can find some inner part, which is uniform and can be treated as the "bulk." This result provides a support for recently proposed core-shell model of large NiO nanoparticles having a size of about 10–18 nm.[46] The structure relaxation influences several atomic layers up to few nanometers below the surface, and also the shape of the initially cubic particle becomes slightly rounded. Note that the relaxation depends also on the nickel atom position at the surface, i.e., in the corner, at the edge or at the face. Adding more vacancies makes this landscape even more complex. Therefore we decided to model nanoparticles as a whole, because it is hard to define any equivalent regions inside the nanoparticle, especially for small particles with nickel vacancies.

We started simulations with a generation of desired NiO model nanoparticles, having a cubic shape, a given size L and a number of randomly distributed Ni vacancies with a given concentration C_{vac}. For each model nanoparticle, we applied previously described MD-EXAFS procedure.

The results of the first step obtained for a large set of nanoparticles are presented in Fig. 9, which shows a value of the residual modulus $|\Delta R(\text{Ni–O}_1)|$ as a function of the particle size L and of the Ni vacancies concentration C_{vac}. One can see that for any size of model nanoparticle starting from $L = 3$ there exists a vacancy concentration that gives for a single Z_{Ni} value both interatomic distances $R(\text{Ni–O}_1)$ and $R(\text{Ni–Ni}_2)$ equal to those found by the conventional modeling procedure (see Fig. 4). This result gives a proof that information from the first two coordination shells is not enough to unambiguously determine both size of and vacancy concentration in a nanoparticle. Nevertheless, this first step allows us to restrict significantly the domain of possible solutions. Therefore it is crucial for the practical implementation, since the calculation of the configuration-averaged EXAFS signal is very time consuming, especially in the case of nanoparticles having many non-equivalent atom sites.

At the second step we considered only those model nanoparticles, which have the average distance in the first $R(\text{Ni–O}_1)$ and second $R(\text{Ni–Ni}_2)$ coordination shells within the desired accuracy (±0.005 Å or better in the present work) compared with the results of the conventional EXAFS analysis (see Sec. II). The configuration-averaged EXAFS spectrum for each nanoparticle was calculated, taking into account the multiple-scattering effects, and the sum of squares of the residuals between the experimental and model EXAFS spectra was evaluated. A small variation of the Ni ions charge Z_{Ni} by ±0.05 was also allowed to further minimize the residual value.

As a result, we found that there is a clear minimum in the dependence of the residual on the particle size and vacancy concentration, which determines the sought model nanoparticle. Thus only comparison between the experimental and configuration-averaged EXAFS spectra, using the full potential of the multiple-scattering theory, allowed us to select the best nanoparticle model, which also fulfills conditions of the first step. The experimental and theoretical EXAFS spectra are compared in Fig. 10, showing good agreement in both k and R space for nanopowder and thin film samples.

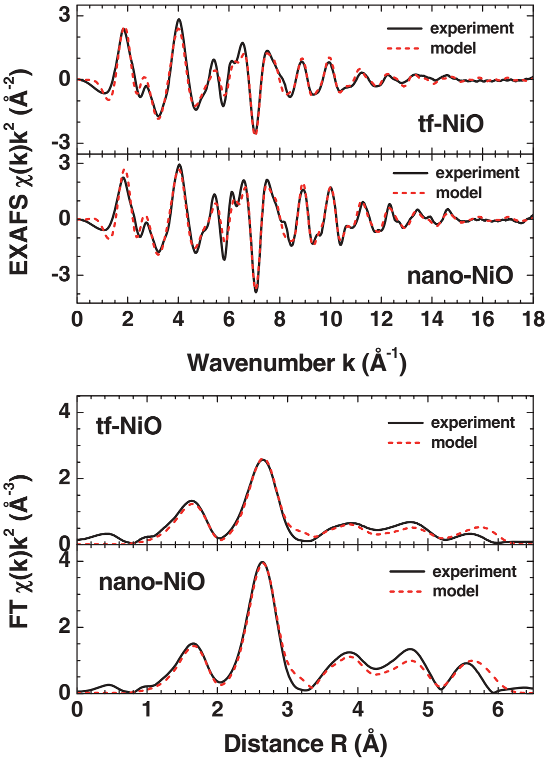

FIG. 10. (Color online) Comparison of the experimental (solid lines) and configuration-averaged (dashed lines) Ni K-edge EXAFS spectra $\chi(k)k^2$ and their Fourier transforms (FTs) for nano-NiO and tf-NiO. The theoretical data correspond to the nanoparticle models that give the best fit to the experimental spectra (nano-NiO: $N = 9$ corresponding to $L \approx 3.6$ nm, $C_{\text{vac}} = 0.4\%$ corresponding to 12 vacancies, $Z_{\text{Ni}} = +1.976$, $Z_{\text{O}} = -1.968$; tf-NiO: $N = 4$ corresponding to $L \approx 1.5$ nm, $C_{\text{vac}} = 1.6\%$ corresponding to four vacancies, $Z_{\text{Ni}} = +1.925$, $Z_{\text{O}} = -1.895$).

The nanoparticle model, having the size $L \approx 3.6$–4.2 nm and the vacancy concentration $C_{\text{vac}} = 0.4$–1.2%, gives the best fit to the experimental EXAFS spectrum for the nanopowder sample (nano-NiO). Applying the same procedure to the thin film sample (tf-NiO), the best agreement was found for the nanoparticle size $L \approx 1.3$–2.1 nm with the vacancy concentration $C_{\text{vac}} = 1.6$–2.0%.

A small discrepancy between the particle size L estimated from EXAFS and that obtained from x-ray diffraction data by the Scherrer's method (4.4–8.0 nm for nano-NiO) can be explained by the simplicity of both models. The largest error comes from the size distribution of nanoparticles, including very small ones that cannot be detected by x-ray diffraction but still give a contribution into the EXAFS signal. This is particulary important for the thin film, taking into consideration the space between grains, which can be filled with very small crystallites or be amorphous.

Finally, we will comment on the structural parameters, obtained by a decomposition of the pair distribution functions from MD simulations into a set of Gaussian functions. Their values for the first six coordination shells of nickel, reported in Table II, show clear evidence of the size reduction and structure relaxation effects. The reduction of the nanoparticle size increases the ratio of atoms at the surface relative to that in the bulk. As a result, a decrease of the average coordination numbers becomes more pronounced in outer coordination shells of both nano-sized samples, as is evidenced by the ratios CN_{na}/CN for the nanopowder and CN_{tf}/CN for the thin film. The atomic structure relaxation appears as a peculiar change of interatomic distances R and an increase of disorder, given by the MSRD σ^2. Note that contrary to our previous works,[47,48] the presence of nickel vacancies in the nanoparticle models allowed us to reproduce simultaneously a decrease of the average nearest-neighbor Ni–O_1 distance and an increase of the outer shell distances. The nickel vacancies along with the nanoparticle surface relaxation contribute also into an increase of the MSRD σ^2 and small decrease of coordination numbers.

Comparing the results obtained from the MD-EXAFS modeling with those from the conventional single-scattering analysis (see Table III), a good agreement is observed in the relative change of interatomic distances for the first two coordination shells of nano-NiO and tf-NiO compared to c-NiO. Note that their absolute values cannot be accurately compared directly, because in our conventional analysis we used experimental amplitude and phase shift functions, which were extracted from the low temperature Ni K-edge EXAFS spectrum of c-NiO assuming the crystallographic value of the lattice parameter $a_0 = 4.176$ Å. The same applies to the MSRDs, those absolute values extracted using the conventional data analysis are influenced by a correlation between the MSRD and coordination number parameters. In addition, the sample quality and the EXAFS amplitude reduction factor (S_0^2) will influence the absolute values as well.[8,14] Nevertheless, the results of the MD-EXAFS and conventional analysis for both relative coordination numbers and relative MSRDs are in agreement showing similar trends (see Table III). The observed differences are attributed mainly to the simplicity of our MD

TABLE II. Structural parameters (CN is the coordination number, R is the interatomic distance, and σ^2 is the MSRD) for the first six coordination shells in c-NiO, nano-NiO, and tf-NiO, calculated by decomposition of the Ni–O and Ni–Ni pair distribution functions, obtained at 300 K, into Gaussian components.

	O_1	Ni_2	O_3	Ni_4	O_5	Ni_6
c-NiO						
CN	6.0	12.0	8.0	6.0	24.0	24.0
R (Å)	2.093	2.961	3.627	4.188	4.682	5.129
σ^2 (Å^2)	0.0055	0.0044	0.0053	0.0058	0.0059	0.0059
nano-NiO						
CN_{na}	5.5	10.5	6.6	5.1	19.8	18.7
R (Å)	2.091	2.968	3.638	4.190	4.685	5.142
σ^2 (Å^2)	0.0072	0.0056	0.0072	0.0093	0.0092	0.0082
tf-NiO						
CN_{tf}	5.1	8.6	5.1	4.1	15.4	12.9
R (Å)	2.091	2.981	3.666	4.193	4.699	5.170
σ^2 (Å^2)	0.0096	0.0083	0.0106	0.0128	0.0140	0.0121
CN_{na}/CN	0.92	0.88	0.83	0.85	0.83	0.78
CN_{tf}/CN	0.85	0.72	0.64	0.68	0.64	0.54

model and to inaccuracies of the theoretical amplitude and phase shift functions.

V. CONCLUSIONS

Extended x-ray absorption fine structure (EXAFS) is a rich source of local structure information, including that on the static and dynamic disorder. However today, the structural data, extracted from the experimental EXAFS spectrum of a compound, are in most cases limited to the first few coordination shells due to difficulties associated with the analysis of multiple-scattering contributions, reflecting the many-atom distribution functions. In the case of nanomaterials, the problem becomes even more complicated due to different factors, related to size reduction, come into play. Therefore the accurate analysis of EXAFS spectra from nanomaterials is challenging.

In this work, we successfully applied a complex modeling approach to the analysis of the Ni K-edge EXAFS in nanosized NiO, having the nanopowder and thin film forms, based on a comparison of the experimental and configuration-averaged EXAFS spectra. The MD-EXAFS method combines classical molecular dynamics with *ab initio* multiple-scattering EXAFS calculations and allows us to account for nanoparticle size and shape, atomic structure relaxation, thermal disorder and the presence of defects (Ni vacancies) using rather simple force-field model, based on the pair potentials and having a few parameters [see Eq. (1)].

TABLE III. Relative to c-NiO values of the structural parameters [CN is the coordination number, R (± 0.002 Å) is the interatomic distance, and σ^2 (± 0.0003 Å^2) is the MSRD] for the first two coordination shells in nano-NiO and tf-NiO, obtained from the best-fit of the EXAFS signals within the Gaussian approximation (see Figs. 3 and 4) and from the MD-EXAFS analysis (see Table II).

	nano-NiO		tf-NiO	
	Gaussian	MD-EXAFS	Gaussian	MD-EXAFS
$Ni\text{-}O_1$				
CN/CN_{c}	1.0	0.92	1.0	0.85
ΔR (Å)	−0.006	−0.002	−0.004	−0.002
$\Delta\sigma^2$ (Å^2)	0.0032	0.0017	0.0061	0.0041
$Ni\text{–}Ni_2$				
CN/CN_{c}	0.92	0.88	0.79	0.72
ΔR (Å)	0.009	0.007	0.017	0.020
$\Delta\sigma^2$ (Å^2)	0.0035	0.0012	0.0068	0.0039

The results of the conventional temperature-dependent EXAFS analysis for the first two coordination shells of nickel atoms provided us with the background information on the modification of the local atomic structure in nanosized NiO compared with microcrystalline NiO. The contraction of the Ni–O_1 bonds and the expansion of the Ni–Ni_2 bonds as well as constantly larger values of the mean-square relative displacement (MSRD) for both bonds were found in nanosized NiO, indicating strong but a particular relaxation of the nanocrystallite atomic structure.

To explain these facts, 3D cubic-shaped nanoparticle models with sizes up to 17 nm were constructed considering the nickel vacancy concentration C_{vac} and the charge of nickel ions Z_{Ni} as variable parameters. After performing MD-EXAFS simulations, the best agreement with the experimental Ni K-edge EXAFS signals was obtained for the nanoparticles with nonzero Ni vacancy concentration ($C_{\text{vac}} \approx 0.4$–1.2% for NiO nanoparticles with the size of $L \approx 3.6$–4.2 nm and $C_{\text{vac}} \approx 1.6$–2.0% for NiO thin film with the size of $L \approx 1.3$–2.1 nm). This result shows that the EXAFS spectroscopy provides a feasible way not only to the size of nanoparticles but also to the concentration of point defects inside them.

The reliability and the applicability range of our MD-EXAFS simulations can be improved and extended in the future by employing more accurate but also computationally much more heavy *ab initio* MD calculations. Such approach will allow one to perform parameter free analysis of the experimental EXAFS data from the first principles, thus disclosing the full potential of the EXAFS method as a tool for complex studies of modern materials (especially nanosized) and for testing theoretical models with high reliability.

ACKNOWLEDGMENTS

The authors are grateful to Dr. Roman Chernikov for assistance during EXAFS measurements at DESY. This work was supported by ESF Project 2009/0202/1DP/1.1.1.2.0/09/APIA/VIAA/141 and Latvian Government Research Grant No. 09.1518. The EXAFS experiments at HASYLAB/DESY have been supported from the European Community's Seventh Framework Programme (FP7/2007-2013) under grant agreement No. 226716 (Project I-20100110 EC).

---

[*] andris.anspoks@cfi.lu.lv

[†] akalin@latnet.lv

[‡] r.kalend@cfi.lu.lv

[§] a.kuzmin@cfi.lu.lv

[1] C. Burda, X. Chen, R. Narayanan, and M. A. El-Sayed, Chem. Rev. **105**, 1025 (2005).

[2] M. Fernández-García, A. Martínez-Arias, J. C. Hanson, and J. A. Rodriguez, Chem. Rev. **104**, 4063 (2004).

[3] S. J. L. Billinge and I. Levin, Science **316**, 516 (2007).

[4] S. C. Ray, J. W. Chiou, W. F. Pong, and M.-H. Tsai, Crit. Rev. Solid State Mater. Sci. **31**, 91 (2006).

[5] S. J. L. Billinge, J. Solid State Chem. **181**, 1695 (2008).

[6] H. Modrow, Appl. Spectroscopy Rev. **39**, 183 (2004).

[7] A. I. Frenkel, A. Yevick, C. Cooper, and R. Vasic, Annu. Rev. Anal. Chem. **4**, 23 (2011).

[8] P. A. Lee, P. H. Citrin, P. Eisenberger, and B. M. Kincaid, Rev. Mod. Phys. **53**, 769 (1981).

[9] G. Dalba, P. Fornasini, R. Grisenti, F. Rocca, D. Comedi, and I. Chambouleyron, Appl. Phys. Lett. **74**, 281 (1999).

[10] V. L. Aksenov, M. V. Kovalchuk, A. Yu. Kuzmin, Yu. Purans, and S. I. Tyutyunnikov, Crystallogr. Rep. **51**, 908 (2006).

[11] S. Larcheri, F. Rocca, F. Jandard, D. Pailharey, R. Graziola, A. Kuzmin, and J. Purans, Rev. Sci. Instrum. **79**, 013702 (2008).

[12] P. Guttmann, C. Bittencourt, S. Rehbein, P. Umek, X. Ke, G. Van Tendeloo, C. P. Ewels, and G. Schneider, Nat. Photon. **6**, 25 (2011).

[13] C. R. Natoli, M. Benfatto, C. Brouder, M. F. RuizLópez, and D. L. Foulis, Phys. Rev. B **42**, 1944 (1990).

[14] J. J. Rehr and R. C. Albers, Rev. Mod. Phys. **72**, 621 (2000).

[15] M. Benfatto, C. R. Natoli, and A. Filipponi, Phys. Rev. B **40**, 9626 (1989).

[16] A. Kuzmin and R. A. Evarestov, J. Phys.: Condens. Matter **21**, 055401 (2009).

[17] A. Kuzmin and R. A. Evarestov, J. Phys.: Conf. Series **190**, 012024 (2009).

[18] A. Kalinko, R. A. Evarestov, A. Kuzmin, and J. Purans, J. Phys.: Conf. Series **190**, 012080 (2009).

[19] J. Timoshenko, A. Kuzmin, and J. Purans, Centr. Eur. J. Phys. **9**, 710 (2011).

[20] A. Kuzmin, V. Efimov, E. Efimova, V. Sikolenko, S. Pascarelli, and I. O. Troyanchuk, Solid State Ionics **188**, 21 (2011).

[21] P. Vashishta, R. K. Kalia, and A. Nakano, J. Nanoparticle Res. **5**, 119 (2003).

[22] M. L. Klein and W. Shinoda, Science **321**, 798 (2008).

[23] K. M. Kim, D. S. Jeong, and C. S. Hwang, Nanotechnology **22**, 254002 (2011).

[24] H. Ohta, M. Hirano, K. Nakahara, H. Maruta, T. Tanabe, M. Kamiya, T. Kamiya, and H. Hosono, Appl. Phys. Lett. **83**, 1029 (2003).

[25] T.-G. Seong, J.-S. Kim, K.-H. Cho, M. K. Yang, W. Kim, J.-K. Lee, J. W. Moon, J. Roh, and S. Nahm, Jpn. J. Appl. Phys. **49**, 121103 (2010).

[26] G. A. Niklasson and C. G. Granqvist, J. Mater. Chem. **17**, 127 (2007).

[27] S. Seo, M. J. Lee, D. H. Seo, E. J. Jeoung, D. S. Suh, Y. S. Joung, I. K. Yoo, I. R. Hwang, S. H. Kim, I. S. Byun, J.-S. Kim, J. S. Choi, and B. H. Park, Appl. Phys. Lett. **85**, 5655 (2004).

[28] T. Suzuki, Z. Hasan, Y. Funahashi, T. Yamaguchi, Y. Fujishiro, and M. Awano, Science **325**, 852 (2009).

[29] C. G. Granqvist, Sol. Energy Mater. Sol. Cells **91**, 1529 (2007).

[30] H. Sato, T. Minami, S. Takata, and T. Yamada, Thin Solid Films **236**, 27 (1993).

[31] O. Kohmoto, H. Nakagawa, Y. Isagawa, and A. Chayahara, J. Magn. Magn. Mater. **226**, 1629 (2001).

[32] J. Yu, K. M. Rosso, and S. M. Bruemmer, J. Phys. Chem. C **116**, 1948 (2012).

[33] A. G. McKale, G. S. Knapp, and S. K. Chan, Phys. Rev. B **33**, 841 (1986).

[34] A. Kuzmin, N. Mironova, J. Purans, and A. Rodionov, J. Phys.: Condens. Matter **7**, 9357 (1995).

[35] R. V. Vedrinskii, V. L. Kraizman, A. A. Novakovich, Sh. M. Elyafi, S. Bocharov, Th. Kirchner, and G. Dräger, Phys. Status Solidi B **226**, 203 (2001).

[36] J. A. Rodriguez, J. C. Hanson, A. I. Frenkel, J. Y. Kim, and M. Perez, J. Am. Chem. Soc. **124**, 346 (2002).

[37] P. Luches, E. Groppo, C. Prestipino, C. Lamberti, C. Giovanardi, and F. Boscherini, Nucl. Instrum. Methods Phys. Res., Sect. B **200**, 371 (2003).

[38] P. Luches, E. Groppo, S. D'Addato, C. Lamberti, C. Prestipino, S. Valeri, and F. Boscherini, Surf. Sci. **566–568**, 84 (2004).

[39] E. Groppo, C. Prestipino, C. Lamberti, R. Carboni, F. Boscherini, P. Luches, S. Valeri, and S. D'Addato, Phys. Rev. B **70**, 165408 (2004).

[40] A. Kuzmin, J. Purans, and A. Rodionov, J. Phys.: Condens. Matter **9**, 6979 (1997).

[41] E. Avendaño, A. Kuzmin, J. Purans, A. Azens, G. A. Niklasson, and C. G. Granqvist, Phys. Scr., T **115**, 464 (2005).

[42] W.-L. Jang, Y.-M. Lu, W.-S. Hwang, T.-L. Hsiung, and H. P. Wang, Appl. Phys. Lett. **94**, 062103 (2009).

[43] W. L. Jang, Y. M. Lu, W. S. Hwang, C. L. Dong, P. H. Hsieh, C. L. Chen, T. S. Chan, and J. F. Lee, Europhys. Lett. **96**, 37009 (2011).

[44] Y. Hattori, T. Konishi, and K. Kaneko, Chem. Phys. Lett. **355**, 37 (2002).

[45] C. T. Meneses, W. H. Flores, and J. M. Sasaki, Chem. Mater. **19**, 1024 (2007).

[46] S. Mandal, S. Banerjee, and K. S. R. Menon, Phys. Rev. B **80**, 214420 (2009).

[47] A. Anspoks, A. Kuzmin, A. Kalinko, and J. Timoshenko, Solid State Commun. **150**, 2270 (2010).

[48] A. Anspoks and A. Kuzmin, J. Non-Cryst. Solids **357**, 2604 (2011).

[49] D. Adler and J. Feinleib, Phys. Rev. B **2**, 3112 (1970).

[50] P. Lunkenheimer, A. Loidl, C. R. Ottermann, and K. Bange, Phys. Rev. B **44**, 5927 (1991).

[51] S. A. Makhlouf, F. T. Parker, F. E. Spada, and A. E. Berkowitz, J. Appl. Phys. **81**, 5561 (1997).

[52] A. Kuzmin, Physica B **208-209**, 175 (1995).

[53] D. Rodic, V. Spasojevic, V. Kusigerski, R. Tellgren, and H. Rundlof, Phys. Status Solidi B **218**, 527 (2000).

[54] J. Purans, A. Kuzmin, E. Cazzanelli, and G. Mariotto, J. Phys.: Condens. Matter **19**, 226206 (2007).

[55] I. T. Todorov, W. Smith, K. Trachenko, and M. T. Dove, J. Mater. Chem. **16**, 1611 (2006).

[56] A. Kuzmin and N. Mironova, J. Phys.: Condens. Matter **10**, 7937 (1998).

[57] C. A. J. Fisher, Scr. Mater. **50**, 1045 (2004).

[58] A. L. Ankudinov, B. Ravel, J. J. Rehr, and S. D. Conradson, Phys. Rev. B **58**, 7565 (1998).

[59] L. Li, L. Chen, R. Qihe, and G. Li, Appl. Phys. Lett. **89**, 134102 (2006).

[60] S. A. Makhlouf, M. A. Kassem, and M. A. Abdel-Rahim, J. Mater. Sci. **44**, 3438 (2009).

[61] H. X. Gao, L. M. Penga, and J. M. Zuo, Acta Crystallogr. Sect. A **55**, 1014 (1999).

[62] T. Okazawa, Y. Nakagawa, and Y. Kido, Phys. Rev. B **69**, 125412 (2004).

[63] B. Bergman and J. Ågren, J. Am. Ceram. Soc. **68**, 444 (1985).

[64] J. A. Hoffmann, A. Paskin, K. J. Tauer, and R. J. Weiss, J. Phys. Chem. Solids **1**, 45 (1956).

[65] A. M. Ferrari and C. Pisani, J. Chem. Phys. **127**, 174711 (2007).

[66] S. Park, H.-S. Ahn, C.-K. Lee, H. Kim, H. Jin, H.-S. Lee, S. Seo, J. Yu, and S. Han, Phys. Rev. B **77**, 134103 (2008).